# Nanoscale Fluid Vortices and Nonlinear Electroosmotic Flow Drive Ion Current Rectification in the Presence of Concentration Gradients

Jake Rabinowitz,[†] Martin A. Edwards,[§] Elizabeth Whittier,[†] Krishna Jayant,[†,‡,∥] and Kenneth L. Shepard*,[†]

[†]Department of Electrical Engineering and [‡]Department of Biological Sciences, Columbia University, New York, New York 10027, United States

[§]Department of Chemistry, University of Utah, Salt Lake City, Utah 84112, United States

S *Supporting Information*

ABSTRACT: Ion current rectification (ICR) is a transport phenomenon in which an electrolyte conducts unequal currents at equal and opposite voltages. Here, we show that nanoscale fluid vortices and nonlinear electroosmotic flow (EOF) drive ICR in the presence of concentration gradients. The same EOF can yield negative differential resistance (NDR), in which current decreases with increasing voltage. A finite element model quantitatively reproduces experimental ICR and NDR recorded across glass nanopipettes under concentration gradients. The model demonstrates that spatial variations of electrical double layer properties induce the nanoscale vortices and nonlinear EOF. Experiments are performed in conditions directly related to scanning probe imaging and show that quantitative understanding of nanoscale transport under concentration gradients requires accounting for EOF. This characterization of nanopipette transport physics will benefit diverse experimentation, pushing the resolution limits of chemical and biophysical recordings.
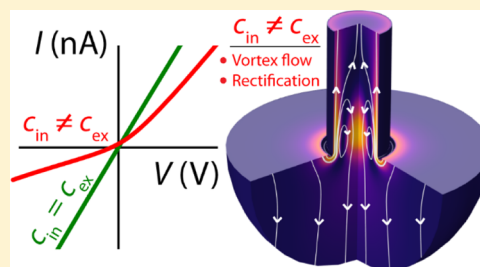
INTRODUCTION

Nanopipettes are tools for studying nanofluidics[1] and probing highly localized signals, with diverse applications in scanning probe microscopy,[2−5] electrophysiology,[6−9] electrochemistry,[10,11] molecular detection,[12−14] chemical delivery,[15,16] and iontophoresis.[17] Across these applications, the smallest pipettes offer the best spatial resolution, and the potential drawback of low current signals can be mitigated by filling pipettes with high-concentration solutions (e.g., 3 M). During experimentation, such pipettes are typically immersed in less concentrated solutions (e.g., 140 mM), creating a concentration gradient at the pipette tip. Because of the concentration gradient, pipettes conduct unequal currents at equal and opposite voltages, favoring one direction of current over the other (see Figure 1)—an effect known as ion current rectification (ICR).[18−25] In this work, we use nanopipettes to characterize ICR in the presence of concentration gradients so that we can properly interpret physical signals recorded under these conditions.

In the case of uniform concentrations, ICR has been extensively studied and characterized.[1,26−30] We refer to the ICR mechanism in these works as Debye-overlap ICR because measurements occur under low-κa conditions, where κa is a dimensionless parameter characterizing the ratio of channel radius (a) to Debye length (κ^{-1}), calculated for a symmetric monovalent electrolyte as $\kappa^{-1} = \sqrt{\frac{\varepsilon k_B T}{2e^2 N_A c^\infty}}$, where ε is solution permittivity, k_B is the Boltzmann constant, e is the elementary charge, N_A is the Avogadro number, and c^∞ is bulk solution concentration. Under low-κa conditions, the electrolyte inside a

charged nanochannel contains an ionic space charge such that the net ion concentration exceeds that of the electroneutral filling solution;[31,32] in the presence of a nanochannel asymmetry (usually, conical shape), this space charge ion concentration can be polarized (e.g., enriched or depleted) with applied voltage, resulting in ICR.[27−30]

Debye-overlap ICR is restricted to intermediate solution concentrations. At low concentrations, the ionic space charge becomes fixed, voltage-induced concentration polarization ceases, and ICR vanishes, with the limiting concentration dependent on the surface charge magnitude in the channel.[33] In the high-κa limit, the Debye length is negligibly small, the ionic space charge no longer contributes appreciably to conduction, and ICR vanishes.[29] By analyzing nanopipette measurements with a finite element model, we elucidate how a concentration gradient overcomes this high-κa ICR limitation.

Under intermediate concentrations (e.g., millimolar), a glass nanopipette exhibits Debye-overlap ICR by conducting more current when negative voltage is applied to the capillary than when positive voltage is applied, with respect to a reference voltage in an external bath solution.[1,27,29,30,34] Taking directional sense from biological ion channels that only permit K^+ influx,[35] we refer to channels conducting more current at negative (positive) voltage as "inward" ("outward") rectifying.
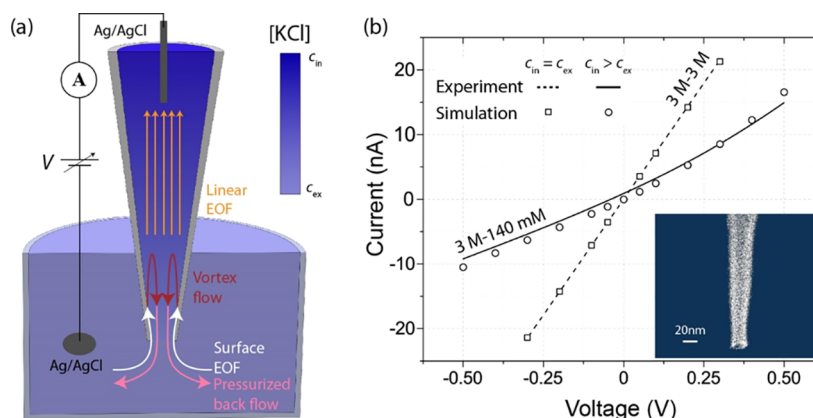
Figure 1. (a) Experimental schematic depicting voltage application and KCl gradient (color), as well as electroosmotic flow (EOF) streamlines, when $V < 0$ V. (b) Experimental (curves) and simulated (symbols) current−voltage recordings for a pipette when $c_{in} = c_{ex} = 3$ M (dashed line, squares) and $c_{in} = 3$ M, $c_{ex} = 140$ mM (solid curve, circles). (Inset) Scanning electron micrograph of representative nanopipette (note: not pipette corresponding to experimental data).

Numerical modeling has verified the Debye-overlap ICR mechanism through calculations of voltage and concentration distributions described by the Poisson and Nernst−Planck equations, respectively.[27−30] Theoretical transport calculations accurately reproduce experimental results with surface charge as the only fitting parameter. Minimal discrepancies are observed when comparing the results of simulations incorporating and ignoring Navier−Stokes physics, demonstrating that EOF does not significantly contribute to Debye-overlap ICR.[29,36−38]

Yet reports of ICR in the presence of concentration or viscosity gradients point to an alternate, EOF-governed ICR mechanism, which we call "flow ICR."[18−25] High-κa ICR[18,21,23,24] and tunable ICR (e.g., inward or outward)[21,22,24] are inconsistent with two corollaries of the Debye-overlap mechanism: (1) ICR should vanish in highly concentrated solutions,[1,29] and (2) surface charge polarity should determine whether a channel is inward or outward rectifying.[34,39] During flow ICR, EOF in the presence of concentration or viscosity gradients results in more conductive solution being driven into or out of the channel, depending on the voltage polarity.[21,24] Under sufficiently large gradients, flow ICR can induce negative differential resistance (NDR), in which an increase in voltage results in a decrease in current.[40,41]

In contrast with Debye-overlap ICR, analyses of flow ICR have yet to thoroughly explain the mechanisms underlying the effect. Extant work either does not reproduce experimental data with a numerical model incorporating EOF[19,21] or neglects EOF within models that only qualitatively match data.[20,22,23] Only twice have simulations reproduced high-κa ICR. In the first case, larger pipettes are considered within a radially independent model (precluding scaling to the low-nanometer range);[42] in the second case, EOF reversal is identified as contributing to flow ICR, but a limited explanation is provided for the observation.[25]

Here, we characterize flow ICR based on agreement between experimental data and simulations showing high-κa ICR, tunable ICR, and NDR in glass nanopipettes under concentration gradients. We investigate the physics governing flow ICR in conditions directly relevant to scanning probe imaging of biological systems by filling pipettes with near-saturated KCl solutions ($c_{in} = 3$ M) and recording currents in physiologically comparable KCl solutions ($c_{ex} = 140$ mM). When reversing the concentration gradient ($c_{in} = 30$ mM, $c_{ex} = 300$ mM), we show that flow ICR can induce NDR. Finite element analysis of the coupled Poisson−Nernst Planck−Navier Stokes equations describes the nonlinear EOF underlying flow ICR, including characteristic nanovortex fluid flows.

METHODS

Pipette Fabrication. Quartz glass capillaries with filaments and 1.0 mm outer and 0.5 mm inner diameters are pulled into nanopipettes using a single step program on a P-2000 micropipette puller: HEAT = 850; FIL = 5; VEL = 55; DEL = 145; PUL = 195. Scanning electron microscopy inspection of many pipettes reveals consistent generation of a nanometer-scale tip. Typical geometry (Figure 1b, inset) is a ~25 nm tip diameter with a cylindrical portion of height ~100 nm, followed by a small-degree conical taper that extends for multiple centimeters.

Experimental Pipette Recordings. After fabrication, pipettes are filled with neutral-buffered KCl solutions and loaded into a micropipette holder containing an internal Ag/AgCl wire electrode. Pipettes are then immersed in an external neutral-buffered KCl solution containing an Ag/AgCl disk electrode. Voltage is applied to the internal wire with respect to the ground reference potential in the external solution (Figure 1a). The pipette voltage is swept using an Axon MultiClamp 700B current amplifier connected to the internal wire through a unity gain headstage. The voltage is swept from −1 to 1 V at a rate of 2 V/s with a 10 kHz sampling rate. During experimentation, five measurements are recorded for a single set of conditions. Displayed data represent the average current values across the sweeps. Error bars are determined from the standard deviations of the recordings and are on the order of the plotted linewidths.

Simulation Theory and Finite Element Modeling. The Poisson (eq S1, "P"), Nernst−Planck (eq S2, "NP"), and Navier−Stokes (eq S3, "NS") equations are evaluated in a cylindrical coordinate system using commercial finite element solver COMSOL Multiphysics 5.3a. The P−NP−NS evaluations describe voltage (P), concentration (NP), and velocity and pressure (NS) profiles inside the nanopipette ($z > 0$) and external solution ($z < 0$). The coupled P−NP−NS equations are self-consistently evaluated with boundary conditions describing experimental conditions. Detailed description and verification of the numerical methods are provided in the Supporting Information Part 1 (Figures S1−S4, Tables S1−S4). A
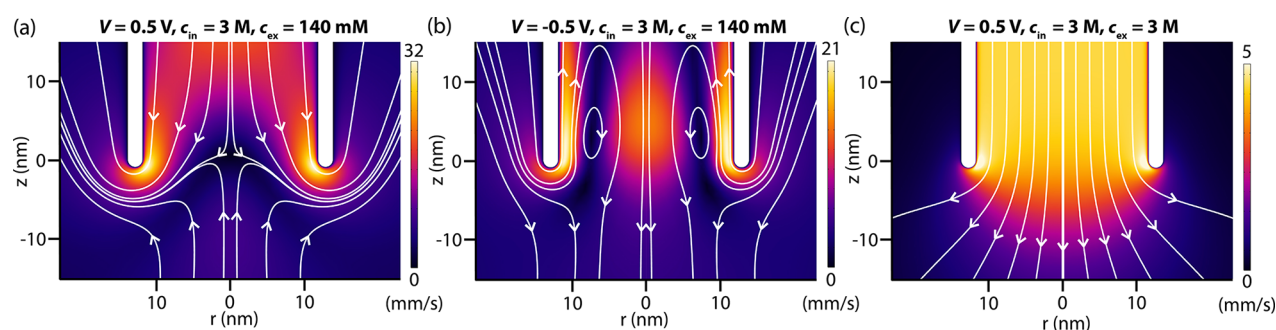
Figure 2. Simulated EOF velocity heatmaps and streamlines at the tip of the pipette in Figure 1b. (a,b) Concentration gradient induces fluid vortices and nonlinear EOF. Vortex shapes are dependent on voltage polarity and are independent of voltage magnitude. (c) Under uniform concentration conditions, no vortex develops. Note that unequal scales are used to visualize flow rates and a concentration gradient increases EOF velocity.

COMSOL-generated report outlining the implementation of the finite element model is provided in the Supporting Information Part 2.

During modeling, pipette geometry (Figure S1) is fit to experimental data based on analytical expressions for electrolyte resistors at high concentrations (eqs S4−S6). The surface charge (σ) is then fit to the measured ICR.

RESULTS AND DISCUSSION

Electroosmosis-Governed ICR When $c_{in} \neq c_{ex}$. When pipette currents are recorded in high-κa conditions with $c_{in} = c_{ex}$ = 3 M, the current−voltage relationship is linear. The pipette of Figure 1b exhibits constant resistance, R_{pip} = 14 MΩ (dashed line). Upon reducing c_{ex} to 140 mM (while maintaining c_{in} = 3 M), the same pipette exhibits a nonlinear current−voltage relation (solid curve), where R_{pip} = 29 MΩ at $V = -0.5$ V and R_{pip} = 52 MΩ at $V = 0.5$ V (noting that R_{pip} increases because of reducing c_{ex}, and voltage-dependent R_{pip} arises because of flow ICR). We quantify ICR with the current rectification ratio (RR), defined as the larger current over the smaller current at $V = \pm 0.5$ V. The pipette of Figure 1b exhibits RR = 1.6 when c_{in} = 3 M and c_{ex} = 140 mM. Recordings from five additional pipettes demonstrate the qualitative consistency of the recordings in Figure 1b, with RR ranging from 1.6−3.4 (Figure S5). Smaller pipettes (larger R_{pip}, Figure S5a) generally rectify more than larger ones (Figure S5b), with variability due to pipette variations during fabrication.

The outward ICR of Figure 1b must be EOF-governed if the pipette surface is negatively charged and measurements are made in high-κa conditions. We confirm negative surface charge by recording pipette currents in less concentrated solutions without concentration gradients, where pipettes exhibit inward Debye-overlap ICR (Figure S6). We confirm high-κa conditions based on concentration-dependent scaling of RR and R_{pip} in the absence of concentration gradients, which indicate a transition from high-κa to low-κa conditions between 3 M and 300 mM (Figure S7).

We further confirm the ICR of Figure 1b to be EOF-governed by measuring both inward and outward ICR across a single pipette, depending on the direction of the concentration gradient (Figure S8). The measured dependence of ICR on the concentration gradient fits our qualitative understanding of flow ICR: when $c_{in} > c_{ex}$, a positive (negative) voltage across a negatively charged channel drives outward (inward) EOF, pushing concentrated (dilute) solution into the channel and decreasing (increasing) resistance.

When fitting a simulation to the pipette in Figure 1b, we determine reasonable values of a = 12 nm and $\sigma = -8$ mC/m^2 (complete parameters provided in Table S2) based on excellent quantitative agreement between simulated current−voltage data (Figure 1b, symbols) and experimental recordings. Within the simulations of Figure 1b, only c_{ex} is altered between the data sets. If EOF is neglected, experimental behavior cannot be reproduced. Relevant EOF streamlines when c_{in} = 3 M, c_{ex} = 140 mM, and $V < 0$ V are qualitatively depicted in Figure 1a.

Fluid Vortices and Nonlinear EOF Drive Flow ICR. We employ the finite element model to further study the EOF inducing experimental ICR. In the presence of the concentration gradient, simulated fluid flow at the tip of the pipette in Figure 1b reveals vortex EOF patterns (Figure 2a,b), a hallmark of nonlinear EOF.[43−49] The flows starkly contrast with the linear EOF pattern observed in the absence of the concentration gradient (Figure 2c). In Figure 2a,b, EOF streamlines depict vortex flows where centerline (r = 0 nm) velocities at the tip oppose EOF near the walls and EOF far into the pipette. We observe that vortex shapes and locations depend on the voltage polarity, pipette geometry, and concentration gradient. As voltage increases, vortices spin faster but do not move.

The vortices and centerline flow reversals result from the combination of fast nonlinear EOF near pipette sidewalls and fluid continuity constraints. When examining the radial velocity distributions across Figure 2, we observe that EOF is fastest along the sidewalls when flow is nonlinear (Figure S9) and fastest at the center when flow is linear (Figure S10). In the nonlinear vortex case, fast EOF along sidewalls at the tip would drive local volumetric fluid flow exceeding the volumetric flow rate far into the pipette, if not for the centerline flow reversal. Thus, the vortex flows ensure that the net volumetric flow rate is equal throughout the pipette, preserving fluid continuity. Further, the nonlinear EOF induced by the concentration gradient increases EOF velocity as compared to uniform concentration conditions (Figure S11). Large hydrostatic pressures develop within the pipette to drive the reversed flows (Figure S12), which we call hydrostatic back flows. The flow reversal mechanism we propose differs from prior explanations of nanopore flow reversals.[25,50]

A concentration gradient induces nonlinear EOF by creating a spatially varying zeta potential, where zeta potential describes the voltage drop across the diffuse part of the electrical double layer.[32] Because this voltage depends on the distance ($\sim 3\kappa^{-1}$) that the diffuse layer extends from the pipette wall, zeta potential is nonuniform in the presence of a concentration gradient. In the absence of a concentration gradient, zeta potential is spatially

uniform and vortex EOF patterns are not observed. Likewise, the two mechanisms for describing nonlinear EOF require spatially varying zeta potentials.[51] In induced charge electroosmosis (ICEO), a voltage polarizes charge along a surface, thereby inducing or exacerbating a nonuniform zeta potential, driving supplemental EOF and culminating in vortex flows.[46,48,49] In electroosmosis of the second kind, a voltage depletes coion concentration at a permselective membrane, thereby inducing or exacerbating a nonuniform zeta potential, compounding the space charge, and culminating in vortex flows.[43−45,47]

In Figure 3a, we simulate the zeta potential along the wall of the pipette. We calculate the zeta potential based on the radial
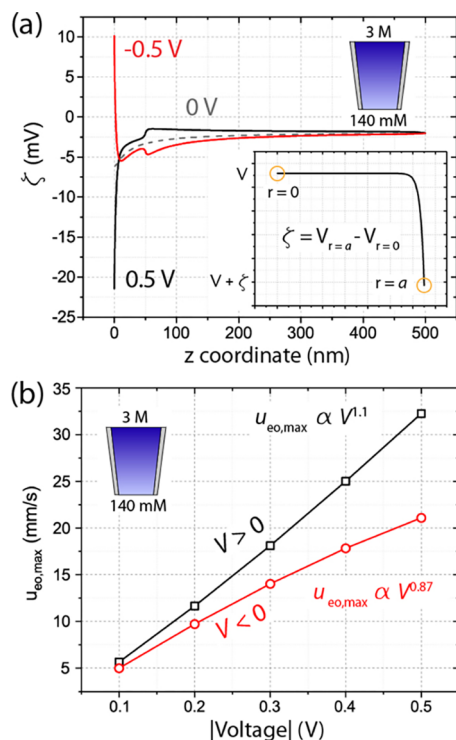

Figure 3. Simulated nonlinear EOF for the pipette in Figure 1b, with c_{in} = 3 M and c_{ex} = 140 mM. (a) Nonuniform zeta potential (ζ) distributions drive nonlinear EOF. When V = 0 V (gray), moderate zeta potential nonuniformity arises due to the concentration gradient. When V = ±0.5 V, induced charge polarization exacerbates zeta potential nonuniformity and drives ICEO. (Inset) Radial voltage distribution showing calculation of zeta potential from simulation. (b) Maximum fluid velocity ($u_{eo,max}$) scales superlinearly with voltage when V > 0 V (black curve) and sublinearly when V < 0 V (red curve), due to the contributions of ICEO flows.

voltage drop between the pipette wall and pipette centerline, as the wall represents the double layer slip plane and the centerline represents a point outside the diffuse part of the double layer. Throughout the simulation domain, the radial voltage profile flattens before the centerline (as shown in the inset), such that the centerline voltage is an appropriate reference against which to measure the zeta potential. With this approach, we follow the conventional definition for zeta potential, while assuming that the Stern layer is coincident with the immobile part of the electrical double layer.[32]

Experimental pipettes exhibit ICEO based on zeta potential nonuniformity, which arises because of the concentration gradient and is exacerbated by induced charge polarization. When c_{in} = 3 M and c_{ex} = 140 mM, in the absence of an electric

field (V = 0), the charged pipette walls and Debye length scaling induce a threefold zeta potential increase between the simulation boundary and pipette tip (Figure 3a, gray curve). When applying V = 0.5 V, the axial electric field induces charge polarization, increasing the negative charge magnitude at the tip and driving a 10-fold zeta potential increase (Figure 3a, black curve). When applying V = −0.5 V, the tip becomes positively charged and zeta potential correspondingly changes sign (Figure 3a, red curve). We further support the ICEO mechanism by quantifying the induced surface charge polarization at the pipette tip (Figure S13). Consistent with the charge polarization, we observe slightly more anions than cations at the tip when V = −0.5 V (Figure S14). Interestingly, the streamlines of Figure 2a,b remain qualitatively consistent with electroosmosis of the second kind in microchannels.[52]

The ICEO fluid velocity (u_{eo}) due to charge polarization superimposes over the linear fluid velocity due to intrinsic pipette charge,[46] with the latter given by the Smoluchowski relation ($u_{eo} = -\varepsilon\zeta E/\eta$, with E as voltage gradient and η as solution viscosity). The cumulative flow yields a power-law relationship between voltage and EOF velocity. In Figure 3b, we quantify EOF nonlinearity by plotting the maximum simulated EOF velocity ($u_{eo,max}$) versus voltage. We find that the vortex flow of Figure 2a yields superlinear velocity scaling as $u_{eo,max} \propto V^{1.1}$ (Figure 3b, black curve), while the vortex flow of Figure 2b yields sublinear velocity scaling as $u_{eo,max} \propto V^{0.87}$ (Figure 3b, red curve). The velocity scaling is consistent with ICEO and the zeta potential distributions of Figure 3a: when V > 0 V, the zeta potential increase drives ICEO flow concurrent to distal EOF, enhancing velocity scaling; when V < 0 V, the zeta potential sign change drives ICEO flow opposing distal EOF, suppressing velocity scaling. Voltage-dependent velocity scaling has previously been reported as EOF rectification.[29,30,53,54]

Scheme 1 provides a qualitative summary of the velocity streamlines in Figure 2a,b and the zeta potential distributions in Figure 3a. In Scheme 1, white streamlines represent ICEO flows along the polarized sidewalls (u_{ICEO}), pink streamlines represent hydrostatic back flows (u_{HBF}) along the center axes, and red streamlines represent vortex mixing flows. The nonuniform zeta potential arises because of spatial variations in Debye length and charge polarization, respectively indicated by the dashed yellow line and symbols within the gray sidewalls (not to scale). Far into the pipette, zeta potential is approximately uniform (Figure 3a), driving linear EOF (qualitatively similar to Figure 2c).

Comparing Flow ICR and Debye-Overlap ICR. Both flow ICR and Debye-overlap ICR arise from voltage-dependent enrichment and depletion of ion concentrations inside a nanochannel. When ICR occurs, reduced resistance is measured for voltages that enrich concentration and increased resistance is measured for voltages that deplete concentration (resistance scales inversely with ion concentration). This effect has been quantified a handful of times during flow ICR[25,42,55] and is well understood during Debye-overlap ICR.[27,29,30]

We quantify ion enrichment and depletion during flow ICR by plotting the concentration distributions for the pipette of Figure 1b with concentration maps (Figure 4a) and centerline profiles (Figure 4b). When V = 0.5 V, outward EOF drives concentrated c_{in} = 3 M solution into the pipette tip, enriching concentration and reducing R_{pip} to 29 MΩ (Figure 4a, left; Figure 4b, black curve). When V = −0.5 V, inward EOF drives dilute c_{ex} = 140 mM solution into the pipette tip, depleting concentration and increasing R_{pip} to 52 MΩ (Figure 4a, right; Figure 4b, red curve). We simulate the same pipette under low-κa conditions, similar

Scheme 1. Characterizing Nonlinear EOF at the Nanopipette Tip[a]

$V = 0.5$ V, $c_{in} = 3$ M, $c_{ex} = 140$ mM

$V = -0.5$ V, $c_{in} = 3$ M, $c_{ex} = 140$ mM
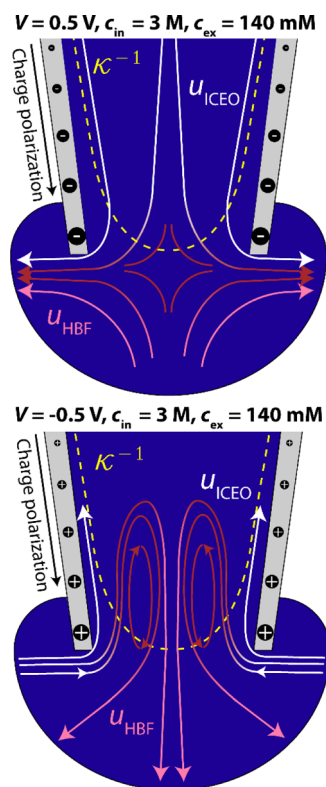
[a]When $c_{in} \neq c_{ex}$, a spatially varying Debye length (dashed yellow line) induces a nonuniform zeta potential. An electric field exacerbates this nonlinearity through induced charge polarization (indicated by sizes and signs of black symbols). Together, the effects drive amplified EOF near sidewalls (u_{ICEO}). In the presence of fast sidewall flow, hydrostatic back flows (u_{HBF}) develop to preserve fluid continuity. Vortex flows (red) connect ICEO and back flow streamlines. Far from the tip, EOF is linear (Figure S9).

to measurements in Figure S6, to illustrate that concentration polarization also underlies Debye-overlap ICR (Figure S15a).

The discrepancies between flow ICR and Debye-overlap ICR are informed by the different mechanisms inducing concentration enrichment and depletion: electroosmosis governs the former and electrophoresis governs the latter. During flow ICR, introducing a solution asymmetry across a channel yields a conductivity gradient, and EOF fills the channel with more or less conductive solution, rectifying current.[21,25,40−42] During Debye-overlap ICR, low-κa conditions yield an ionic space charge in the channel and a geometric asymmetry introduces voltage-dependent transport restrictions, rectifying current.[1,27−29,31] In flow ICR, surface charge is required to induce EOF, while in Debye-overlap ICR, surface charge is required to induce a space charge electrolyte; in both, an asymmetry is required to yield voltage-dependent resistance. These qualities of flow ICR and Debye-overlap ICR, including the consequences of the disparate mechanisms, are compared in Scheme 2.

A useful outcome of the concentration gradient in flow ICR is control over ion transport selectivity,[55] as shown in Figure S16. During flow ICR when $c_{in} > c_{ex}$, both ions diffuse from the pipette and the voltage can be set to draw in as many ions as exit via diffusion. For example, when $V \approx -80$ mV, voltage-driven influx of K$^+$ opposes diffusive efflux, such that the current from the
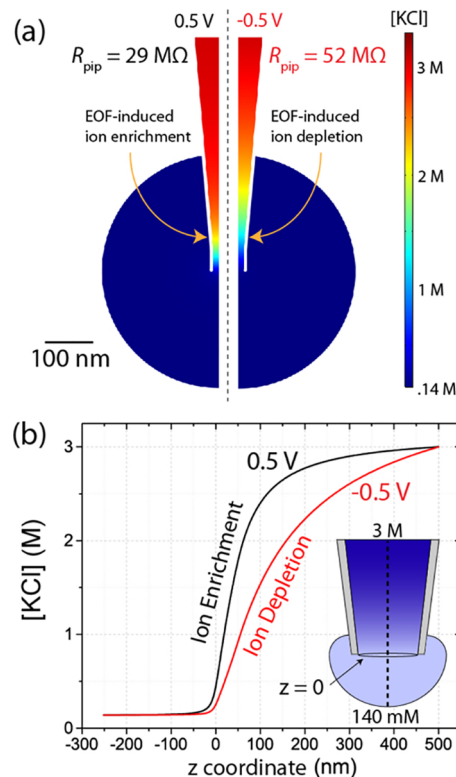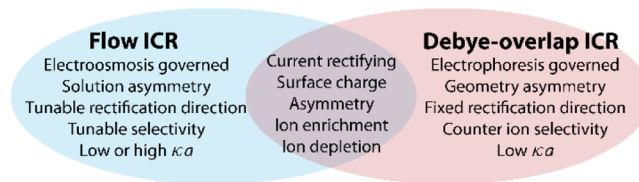

Figure 4. Simulated ion distributions for the pipette in Figure 1b, when $c_{in} = 3$ M and $c_{ex} = 140$ mM. (a) Concentration maps and (b) centerline profiles, when $V = \pm 0.5$ V. Voltage-dependent ion concentration enrichment and depletion arise because of EOF, inducing ICR. Space charge is negligible, such that [K$^+$] = [Cl$^-$] = [KCl].

Scheme 2. Comparison of Flow and Debye-Overlap ICR

pipette in Figure 1b is primarily comprised of Cl$^-$. During scanning probe imaging of neurons, the ability to tune ionic selectivity is particularly beneficial, as large K$^+$ flux will desensitize membrane ion channels but Cl$^-$ flux is less detrimental.[56] In contrast, the space charge within the Debye-overlap ICR pipette (Figure S15b) results in preferential transport of cations throughout experimental voltages, though precise selectivity does vary with voltage (Figure S16).

EOF Influences Transport Amidst Concentration Gradients. Extended simulations show that EOF influences transport for all moderate surface charge conditions in the presence of mismatched millimolar and molar concentrations. In Figure 5a, we compare current−voltage simulations incorporating EOF (P−NP−NS, symbols) and ignoring EOF (P−NP, curves) for the pipette of Figure 1b ($c_{in} = 3$ M, $c_{ex} = 140$ mM) across a range of surface charges ($\sigma = -40$ to 40 mC/m^2). These surface charge modifications are achievable through chemical treatment of the glass capillary. Figure 5b shows analogous simulations with the concentrations inverted ($c_{in} = 140$ mM, $c_{ex} = 3$ M). For both concentration gradient directions, ignoring EOF inverts the relationship between surface charge polarity
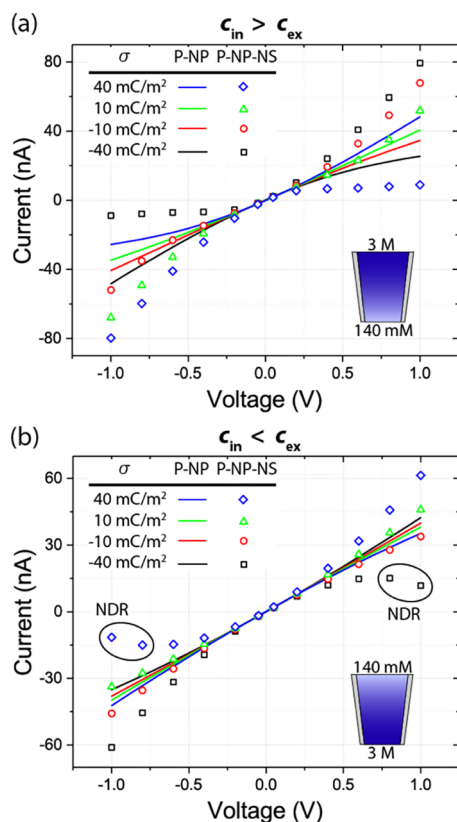
Figure 5. Simulated pipette current−voltage relationships with (symbols, P−NP−NS) and without (curves, P−NP) EOF, when sweeping surface charge (σ), with (a) $c_{in} > c_{ex}$ and (b) $c_{in} < c_{ex}$. Simulations ignoring EOF invert the relationship between ICR and surface charge polarity and underestimate RR. (b) Vortex flows can induce NDR under sufficient voltage and surface charge. When $c_{in} = c_{ex}$, ignoring EOF is valid (Figure S18).

and ICR direction and underestimates RR due to losing ICEO transport. Thus, if EOF is not considered during modeling of experimental transport in the presence of a concentration gradient, it is likely to misrepresent surface charge polarity.

Across a larger range of κa conditions and concentration gradients, we similarly find that EOF influences transport (Figure S17). When simulating current−voltage relations for pipettes with c_{in} and c_{ex} ranging from 3 M to 3 mM, ignoring EOF yields quantitative disagreement across all conditions and often inverts the predicted direction of ICR. Accordingly, EOF must be included to quantitatively model experimental transport recorded amidst concentration gradients. Upon removing the concentration gradient, EOF negligibly influences transport when $c_{in} = c_{ex} = 3$ M and $c_{in} = c_{ex} = 140$ mM (Figure S18).

NDR when $c_{in} < c_{ex}$. NDR is an ICR-related phenomenon in which an increase in voltage is accompanied by a decrease in current. Two prior reports of NDR measured under viscosity[40] and concentration ($c_{in} > c_{ex}$)[41] gradients required external pressure. The latter proposed exploiting NDR for chemical sensing. Elsewhere, reports of NDR required high voltages[49,57] or low concentration and current levels.[58] In Figure 5b, we highlight the predictions that when $c_{in} < c_{ex}$, flow ICR can induce NDR in conditions distinct from these prior works, albeit at surface charge levels higher than those observed experimentally. Because increasing surface charge reduces the ratio of ions in the electroneutral solution to ions in the diffuse double layer, we

reproduce the simulated NDR through lowering the experimental κa while maintaining $c_{in} < c_{ex}$.

When pipette currents are recorded with $c_{in} = 30$ mM and $c_{ex} = 300$ mM, we measure NDR in the $V = 0.6-1.0$ V range, as shown in Figure 6a (curve). The measured NDR agrees with
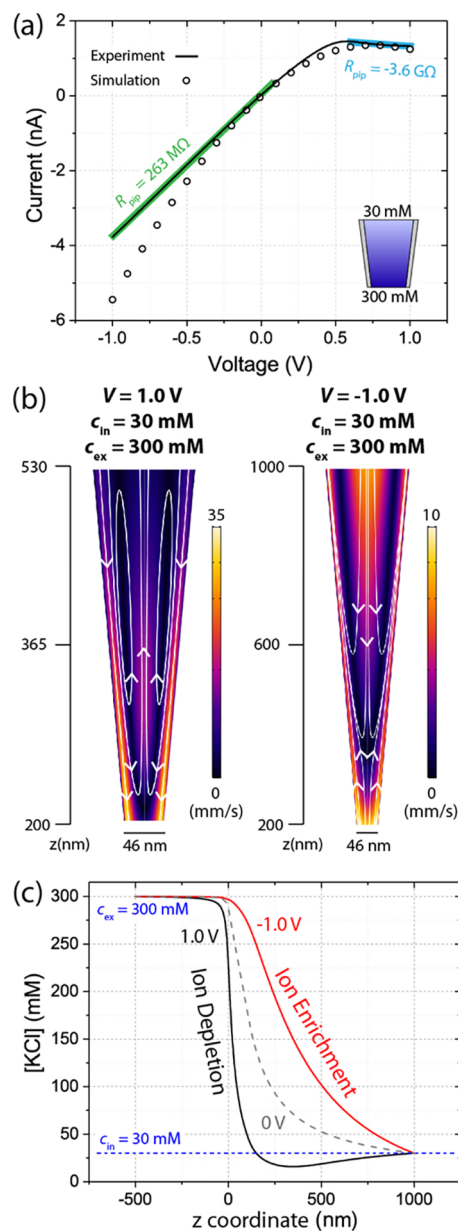

Figure 6. (a) Experimental (line) and simulated (symbols) NDR for a pipette when $c_{in} = 30$ mM and $c_{ex} = 300$ mM. (b) Simulated EOF velocity heatmaps and streamlines for the pipette in (a). When $V = 1.0$ V (left), the vortex flows induce NDR. (c) Simulated centerline concentrations for the pipette in (a). EOF enriches (red) or depletes (black) concentration; during NDR, depletion reduces internal concentration below the levels of the filling solutions.

simulations for a pipette with $a = 15$ nm and $\sigma = -12$ mC/m² (Figure 6a, circles; complete parameters provided in Table S2). Moderate variations in surface charge across experimental SiO$_2$ devices have been observed previously,[59,60] and we attribute our increase in surface charge to fabrication variability. Simulations indicate that NDR occurs only at certain combinations of geometry and surface charge (Figure S19), consistent with

referenced work[41] and experimental NDR being recorded in only 3 of ~30 pipettes tested with c_{in} = 30 mM and c_{ex} = 300 mM.

Mechanistically, NDR is attributed to the influence of the vortex flow pattern on ion concentrations. It can thus be considered a natural extension of the flow ICR discussion. In Figure 6b, we depict simulated fluid velocity heatmaps and streamlines at the tip of the pipette in Figure 6a, where the ICEO streamlines near the wall (see u_{ICEO}, Scheme 1) carry ion-enriched diffuse double layer fluid (Figure S20). As voltage increases and vortices spin faster, the hydrostatic back flows (see u_{HBF}, Scheme 1) progressively deplete ions to preserve mass continuity, analogous to the fluid continuity arguments made previously.

The vortex flow pattern induces NDR when the hydrostatic back flows deplete ion concentrations within the pipette below the levels of the filling solutions. The concentration depletion is depicted in Figure 6c, which shows simulated concentration distributions for the pipette of Figure 6a. When V = 1.0 V, the intermediate pipette concentration reduces below c_{in} (Figure 6c, black curve), an effect that does not occur in simulation until EOF is sufficiently fast (V = 0.8 V, Figure S21) and coincides with the onset of NDR. When the internal pipette concentration depletes below the levels of the filling solutions, the low-concentration region displaces the small tip aperture as the greatest contributor to resistance and NDR is measured.

Simulated zeta potential distributions for the pipette in Figure 6a show severe nonuniformity (Figure 7a), as expected. The profiles are consistent with the vortex locations in Figure 6b, which are much further into the pipette than those of Figure

2a,b. When V = 1.0 V (black curve), negative charge polarization induces a zeta potential maximum at $z \approx 350$ nm, near the center of the vortex flow in Figure 6b (left). When V = −1.0 V (red curve), positive charge polarization results in a zeta potential maximum at the simulation boundary (z = 1000 nm), around which the vortex flow remains centered. It is therefore conceivable to engineer systems with carefully placed vortex flows, with possible applications in nanoscale mixing or single molecule trapping, if a surface can be selectively patterned with a charged coating.[61] Downstream of the internal vortices, flow is linear (Figure S22).

We lastly demonstrate that EOF rectification is responsible for the pipette of Figure 6a only exhibiting NDR when V > 0 V. In Figure 7b, we simulate the maximum EOF velocity ($u_{eo,max}$) versus voltage, observing EOF rectification with exacerbated nonlinearity as compared to Figure 3b. Through the NDR regime (V > 0, black curve), velocity scales superlinearly as $u_{eo,max} \propto V^{1.62}$. Through the more conductive regime (V < 0, red curve), velocity scales sublinearly as $u_{eo,max} \propto V^{0.82}$. The sublinear EOF scaling prevents the vortex from spinning fast enough for hydrostatic back flows to deplete internal ion concentrations below the levels of the filling solutions.

We note that the velocity scaling of Figure 7b is qualitatively consistent with charge polarization in Figure 7a and comparable measurements when c_{in} > c_{ex} (Figure 3b). These similarities indicate that a negatively charged surface in the presence of a concentration gradient can be expected to exhibit EOF rectification with higher flow rates for positive voltages, independent of the direction of the concentration gradient, because of the induced charge effect.

■ CONCLUSIONS

We characterize EOF-governed ICR ("flow ICR") through quantitative agreement between experimental and simulated current−voltage relationships for nanopipettes under concentration gradients. During flow ICR, current rectifies based on EOF driving more or less concentrated solution into the nanochannel, with a preferred current direction that is tunable and inverts with the concentration gradient. We demonstrate that the concentration gradient and surface charge polarization induce a spatially varying zeta potential that drives nanoscale fluid vortices, nonlinear EOF, and EOF rectification. The same mechanisms can result in NDR when vortex flows thoroughly deplete ion concentrations inside the nanochannel. Through simulations, we show that for millimolar and/or molar solutions, EOF influences ion and fluid transport in the presence of any concentration gradient.

The effects studied herein are applicable to many nanopipette applications. In scanning probe microscopy and electrophysiology, filling pipettes with highly concentrated solutions improves the signal-to-noise ratio but could distort signals if these nonlinear effects are not considered. In electrochemistry and molecular detection, concentration gradients can facilitate localized concentration enrichment or depletion of desired analytes. In chemical delivery and iontophoresis, concentration gradients can improve transport efficiency and selectivity. Further, exploitation of the vortex flows we present may afford additional opportunities in nanoscale mixing.

Finally, we speculate that these mechanisms may contribute to intracellular rectification of ion and fluid transport. Though our experiments contain many simplifications compared to natural systems, the voltage and concentration gradients considered in this work are comparable to those found in
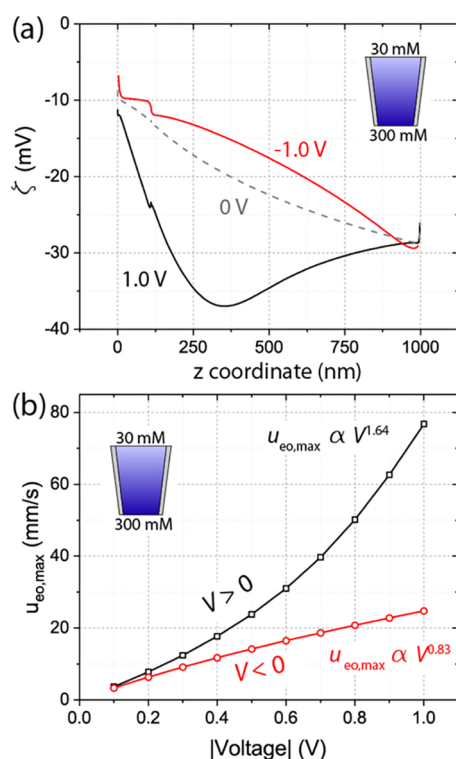

Figure 7. Simulated nonlinear EOF for the pipette in Figure 6a (c_{in} = 30 mM, c_{ex} = 300 mM). (a) Zeta potential (ζ) distribution when V = 1.0 V (black), 0 V (gray), and −1.0 V (red). Vortex flows in Figure 6b center around zeta potential maxima. (b) Maximum fluid velocity ($u_{eo,max}$) scales superlinearly with voltage when V > 0 V (black curve) and sublinearly when V < 0 V (red curve).

certain cells. For example, during synaptic integration, large spatial ionic gradients are known to occur across the dendritic spine apparatus,[62] conditions where nonlinear EOF may contribute to the ensuing ion transport and voltage dynamics.

■ ASSOCIATED CONTENT

ⓈSupporting Information

The Supporting Information is available free of charge on the ACS Publications website at DOI: 10.1021/acs.jpca.9b04075.

> Simulation theory and verification, experimental pipette characterization, and supplemental analysis (PDF)
>
> COMSOL-generated report describing finite element model implementation (PDF)

■ AUTHOR INFORMATION

Corresponding Author

*E-mail: shepard@ee.columbia.edu (K.S.).

ORCID

Jake Rabinowitz: 0000-0001-9671-6860

Martin A. Edwards: 0000-0001-8072-361X

Present Address

∥Department of Biomedical Engineering, Purdue University, West Lafayette, IN 47906, USA.

Notes

The authors declare no competing financial interest.

■ ACKNOWLEDGMENTS

■ REFERENCES

(1) Wei, C.; Bard, A. J.; Feldberg, S. W. Current Rectification at Quartz Nanopipet Electrodes. *Anal. Chem.* **1997**, *69*, 4627−4633.

(2) Novak, P.; Li, C.; Shevchuk, A. I.; Stepanyan, R.; Caldwell, M.; Hughes, S.; Smart, T. G.; Gorelik, J.; Ostanin, V. P.; Lab, M. J.; et al. Nanoscale Live-Cell Imaging Using Hopping Probe Ion Conductance Microscopy. *Nat. Methods* **2009**, *6*, 279−281.

(3) McKelvey, K.; Kinnear, S. L.; Perry, D.; Momotenko, D.; Unwin, P. R. Surface Charge Mapping with a Nanopipette. *J. Am. Chem. Soc.* **2014**, *136*, 13735−13744.

(4) Perry, D.; Page, A.; Chen, B.; Frenguelli, B. G.; Unwin, P. R. Differential-Concentration Scanning Ion Conductance Microscopy. *Anal. Chem.* **2017**, *89*, 12458−12465.

(5) Choi, M.; Baker, L. A. Biphasic-Scanning Ion Conductance Microscopy. *Anal. Chem.* **2018**, *90*, 11797−11801.

(6) Schrlau, M. G.; Dun, N. J.; Bau, H. H. Cell Electrophysiology with Carbon Nanopipettes. *ACS Nano* **2009**, *3*, 563−568.

(7) Novak, P.; Gorelik, J.; Vivekananda, U.; Shevchuk, A. I.; Ermolyuk, Y. S.; Bailey, R. J.; Bushby, A. J.; Moss, G. W. J.; Rusakov, D. A.; Klenerman, D.; et al. Nanoscale-Targeted Patch-Clamp Recordings of Functional Presynaptic Ion Channels. *Neuron* **2013**, *79*, 1067−1077.

(8) Jayant, K.; Hirtz, J. J.; Plante, I. J.-L.; Tsai, D. M.; De Boer, W. D. A. M.; Semonche, A.; Peterka, D. S.; Owen, J. S.; Sahin, O.; Shepard, K. L.; et al. Targeted Intracellular Voltage Recordings from Dendritic Spines Using Quantum-Dot-Coated Nanopipettes. *Nat. Nanotechnol.* **2017**, *12*, 335−342.

(9) Jayant, K.; Wenzel, M.; Bando, Y.; Hamm, J. P.; Mandriota, N.; Rabinowitz, J. H.; Plante, I. J.-L.; Owen, J. S.; Sahin, O.; Shepard, K. L.; et al. Flexible Nanopipettes for Minimally Invasive Intracellular Electrophysiology In Vivo. *Cell Rep.* **2019**, *26*, 266−278.

(10) Mirkin, M. V.; Fan, F.-R. F.; Bard, A. J. Direct Electrochemical Measurements inside a 2000 Angstrom Thick Polymer Film by Scanning Electrochemical Microscopy. *Science* **1992**, *257*, 364−366.

(11) Shao, Y.; Mirkin, M. V.; Fish, G.; Kokotov, S.; Palanker, D.; Lewis, A. Nanometer-Sized Electrochemical Sensors. *Anal. Chem.* **1997**, *69*, 1627−1634.

(12) Karhanek, M.; Kemp, J. T.; Pourmand, N.; Davis, R. W.; Webb, C. D. Single DNA Molecule Detection Using Nanopipettes and Nanoparticles. *Nano Lett.* **2005**, *5*, 403−407.

(13) Piper, J. D.; Clarke, R. W.; Korchev, Y. E.; Ying, L.; Klenerman, D. A Renewable Nanosensor Based on a Glass Nanopipette. *J. Am. Chem. Soc.* **2006**, *128*, 16462−16463.

(14) Umehara, S.; Karhanek, M.; Davis, R. W.; Pourmand, N. Label-Free Biosensing with Functionalized Nanopipette Probes. *Proc. Natl. Acad. Sci. U.S.A.* **2009**, *106*, 4611−4616.

(15) Wang, Y.; Cai, H.; Mirkin, M. V. Delivery of Single Nanoparticles from Nanopipettes under Resistive-Pulse Control. *ChemElectroChem* **2015**, *2*, 343−347.

(16) McKelvey, K.; Edwards, M. A.; White, H. S. Resistive Pulse Delivery of Single Nanoparticles to Electrochemical Interfaces. *J. Phys. Chem. Lett.* **2016**, *7*, 3920−3924.

(17) Herr, N. R.; Kile, B. M.; Carelli, R. M.; Wightman, R. M. Electroosmotic Flow and Its Contribution to Iontophoretic Delivery. *Anal. Chem.* **2008**, *80*, 8635−8641.

(18) Fåhraeus, C.; Borglid, K.; Grampp, W. Properties of Electrolyte-Filled Glass Microelectrodes: An Experimental Study. *J. Neurosci. Methods* **1997**, *78*, 15−28.

(19) Siwy, Z.; Fuliński, A. A Nanodevice for Rectification and Pumping Ions. *Am. J. Phys.* **2004**, *72*, 567−574.

(20) Cheng, L.-J.; Guo, L. J. Rectified Ion Transport through Concentration Gradient in Homogeneous Silica Nanochannels. *Nano Lett.* **2007**, *7*, 3165−3171.

(21) Yusko, E. C.; An, R.; Mayer, M. Electroosmotic Flow Can Generate Ion Current Rectification in Nano- and Micropores. *ACS Nano* **2010**, *4*, 477−487.

(22) Cao, L.; Guo, W.; Wang, Y.; Jiang, L. Concentration-Gradient-Dependent Ion Current Rectification in Charged Conical Nanopores. *Langmuir* **2012**, *28*, 2194−2199.

(23) Deng, X. L.; Takami, T.; Son, J. W.; Kang, E. J.; Kawai, T.; Park, B. H. Effect of Concentration Gradient on Ionic Current Rectification in Polyethylenimine Modified Glass. *Sci. Rep.* **2014**, *4*, 4005.

(24) Qiu, Y.; Lucas, R. A.; Siwy, Z. S. Viscosity and Conductivity Tunable Diode-like Behavior for Meso- and Micropores. *J. Phys. Chem. Lett.* **2017**, *8*, 3846−3852.

(25) Qiu, Y.; Siwy, Z. S.; Wanunu, M. Abnormal Ionic-Current Rectification Caused by Reversed Electroosmotic Flow under Viscosity Gradients across Thin Nanopores. *Anal. Chem.* **2019**, *91*, 996−1004.

(26) Siwy, Z.; Fuliński, A. Fabrication of a Synthetic Nanopore Ion Pump. *Phys. Rev. Lett.* **2002**, *89*, 198103.

(27) Woermann, D. Electrochemical Transport Properties of a Cone-Shaped Nanopore: High and Low Electrical Conductivity States Depending on the Sign of an Applied Electrical Potential Difference. *Phys. Chem. Chem. Phys.* **2003**, *5*, 1853−1858.

(28) Cervera, J.; Schiedt, B.; Ramírez, P. A Poisson/Nernst-Planck Model for Ionic Transport through Synthetic Conical Nanopores. *Europhys. Lett.* **2005**, *71*, 35−41.

(29) White, H. S.; Bund, A. Ion Current Rectification at Nanopores in Glass Membranes. *Langmuir* **2008**, *24*, 2212−2218.

(30) Lan, W.-J.; Edwards, M. A.; Luo, L.; Perera, R. T.; Wu, X.; Martin, C. R.; White, H. S. Voltage-Rectified Current and Fluid Flow in Conical Nanopores. *Acc. Chem. Res.* **2016**, *49*, 2605−2613.

(31) Plecis, A.; Schoch, R. B.; Renaud, P. Ionic Transport Phenomena in Nanofluidics: Experimental and Theoretical Study of the Exclusion-Enrichment Effect on a Chip. *Nano Lett.* **2005**, *5*, 1147−1155.

(32) Schoch, R. B.; Han, J.; Renaud, P. Transport Phenomena in Nanofluidics. *Rev. Mod. Phys.* **2008**, *80*, 839−883.

(33) Cervera, J.; Schiedt, B.; Neumann, R.; Mafé, S.; Ramírez, P. Ionic Conduction, Rectification, and Selectivity in Single Conical Nanopores. *J. Chem. Phys.* **2006**, *124*, 104706.

(34) Umehara, S.; Pourmand, N.; Webb, C. D.; Davis, R. W.; Yasuda, K.; Karhanek, M. Current Rectification with Poly-L-Lysine-Coated Quartz Nanopipettes. *Nano Lett.* **2006**, *6*, 2486–2492.

(35) Kubo, Y.; Baldwin, T. J.; Nung Jan, Y.; Jan, L. Y. Primary Structure and Functional Expression of a Mouse Inward Rectifier Potassium Channel. *Nature* **1993**, *362*, 127–133.

(36) Ai, Y.; Zhang, M.; Joo, S. W.; Cheney, M. A.; Qian, S. Effects of Electroosmotic Flow on Ionic Current Rectification in Conical Nanopores. *J. Phys. Chem. C* **2010**, *114*, 3883–3890.

(37) Lin, D.-H.; Lin, C.-Y.; Tseng, S.; Hsu, J.-P. Influence of Electroosmotic Flow on the Ionic Current Rectification in a PH-Regulated, Conical Nanopore. *Nanoscale* **2015**, *7*, 14023–14031.

(38) Hsu, J.-P.; Yang, S.-T.; Lin, C.-Y.; Tseng, S. Ionic Current Rectification in a Conical Nanopore: Influences of Electroosmotic Flow and Type of Salt. *J. Phys. Chem. C* **2017**, *121*, 4576–4582.

(39) Siwy, Z.; Heins, E.; Harrell, C. C.; Kohli, P.; Martin, C. R. Conical-Nanotube Ion-Current Rectifiers: The Role of Surface Charge. *J. Am. Chem. Soc.* **2004**, *126*, 10850–10851.

(40) Luo, L.; Holden, D. A.; Lan, W.-J.; White, H. S. Tunable Negative Differential Electrolyte Resistance in a Conical Nanopore in Glass. *ACS Nano* **2012**, *6*, 6507–6514.

(41) Luo, L.; Holden, D. A.; White, H. S. Negative Differential Electrolyte Resistance in a Solid-State Nanopore Resulting from Electroosmotic Flow Bistability. *ACS Nano* **2014**, *8*, 3023–3030.

(42) Fåhraeus, C.; Grampp, W. Properties of Electrolyte-Filled Glass Microelectrodes: A Model Analysis. *J. Neurosci. Methods* **1997**, *78*, 29–45.

(43) Dukhin, S. S. Electrokinetic Phenomena of the Second Kind and Their Applications. *Adv. Colloid Interface Sci.* **1991**, *35*, 173–196.

(44) Rubinstein, I.; Zaltzman, B. Electro-Osmotically Induced Convection at a Permselective Membrane. *Phys. Rev. E: Stat. Phys., Plasmas, Fluids, Relat. Interdiscip. Top.* **2000**, *62*, 2238–2251.

(45) Ben, Y.; Chang, H.-C. Nonlinear Smoluchowski Slip Velocity and Micro-Vortex Generation. *J. Fluid Mech.* **2002**, *461*, 229–238.

(46) Squires, T. M.; Bazant, M. Z. Induced-Charge Electro-Osmosis. *J. Fluid Mech.* **2004**, *509*, 217–252.

(47) Kim, S. J.; Wang, Y.-C.; Lee, J. H.; Jang, H.; Han, J. Concentration Polarization and Nonlinear Electrokinetic Flow near a Nanofluidic Channel. *Phys. Rev. Lett.* **2007**, *99*, 044501.

(48) Gregersen, M. M.; Andersen, M. B.; Soni, G.; Meinhart, C.; Bruus, H. Numerical Analysis of Finite Debye-Length Effects in Induced-Charge Electro-Osmosis. *Phys. Rev. E: Stat., Nonlinear, Soft Matter Phys.* **2009**, *79*, 066316.

(49) Park, S.; Yossifon, G. Induced-Charge Electrokinetics, Bipolar Current, and Concentration Polarization in a Microchannel-Nafion-Membrane System. *Phys. Rev. E* **2016**, *93*, 062614.

(50) Laohakunakorn, N.; Thacker, V. V.; Muthukumar, M.; Keyser, U. F. Electroosmotic Flow Reversal Outside Glass Nanopores. *Nano Lett.* **2015**, *15*, 695–702.

(51) Bazant, M. Z. *Encyclopedia of Microfluidics and Nanofluidics*; Li, D., Ed.; Springer: New York, 2015; pp 2416–2426.

(52) Dydek, E. V.; Zaltzman, B.; Rubinstein, I.; Deng, D. S.; Mani, A.; Bazant, M. Z. Overlimiting Current in a Microchannel. *Phys. Rev. Lett.* **2011**, *107*, 118301.

(53) Jin, P.; Mukaibo, H.; Horne, L. P.; Bishop, G. W.; Martin, C. R. Electroosmotic Flow Rectification in Pyramidal-Pore Mica Membranes. *J. Am. Chem. Soc.* **2010**, *132*, 2118–2119.

(54) Laohakunakorn, N.; Keyser, U. F. Electroosmotic Flow Rectification in Conical Nanopores. *Nanotechnology* **2015**, *26*, 275202.

(55) Yeh, L.-H.; Hughes, C.; Zeng, Z.; Qian, S. Tuning Ion Transport and Selectivity by a Salt Gradient in a Charged Nanopore. *Anal. Chem.* **2014**, *86*, 2681–2686.

(56) Hill, R. W.; Wyse, G. A.; Anderson, M. *Animal Physiology*; Sinauer Associates: Sunderland, 2012.

(57) Yossifon, G.; Mushenheim, P.; Chang, Y.-C.; Chang, H.-C. Nonlinear Current-Voltage Characteristics of Nanochannels. *Phys. Rev. E: Stat., Nonlinear, Soft Matter Phys.* **2009**, *79*, 046305.

(58) Cheng, L.-J.; Guo, L. J. Ionic Current Rectification, Breakdown, and Switching in Heterogeneous Oxide Nanofluidic Devices. *ACS Nano* **2009**, *3*, 575–584.

(59) Schoch, R. B.; Renaud, P. Ion Transport through Nanoslits Dominated by the Effective Surface Charge. *Appl. Phys. Lett.* **2005**, *86*, 253111.

(60) Karnik, R.; Fan, R.; Yue, M.; Li, D.; Yang, P.; Majumdar, A. Electrostatic Control of Ions and Molecules in Nanofluidic Transistors. *Nano Lett.* **2005**, *5*, 943–948.

(61) Stroock, A. D.; Whitesides, G. M. Controlling Flows in Microchannels with Patterned Surface Charge and Topography. *Acc. Chem. Res.* **2003**, *36*, 597–604.

(62) Lagache, T.; Jayant, K.; Yuste, R. Electrodiffusion Model of Synaptic Potentials in Dendritic Spines. **2018**, bioRxiv, 274373.